Journal of Hydrology 521 (2015) 286–301

Contents lists available at ScienceDirect

Journal of Hydrology

journal homepage: www.elsevier.com/locate/jhydrol

# Passive electrical monitoring and localization of fluid leakages from wells

A. Revil [a,b,*], D. Mao [a], A.K. Haas [c], M. Karaoulis [d], L. Frash [e]

[a] Colorado School of Mines, Dept. of Geophysics, Green Center, 1500 Illinois Street, 80401 Golden, CO, USA
[b] ISTerre, CNRS, UMR CNRS 5275, Université de Savoie, 73376 Le Bourget du Lac cedex, France
[c] Hydrogeophysics, Inc., USA
[d] Deltares, The Netherlands
[e] Colorado School of Mines, Dept. of Civil & Environmental Engineering, 1500 Illinois Street, 80401 Golden, CO, USA

ARTICLE INFO

*Article history:*
Received 16 September 2014
Received in revised form 2 December 2014
Accepted 3 December 2014
Available online 11 December 2014
This manuscript was handled by Peter K. Kitanidis, Editor-in-Chief, with the assistance of J.A. Huisman, Associate Editor

*Keywords:*
Pumping test
Leakage
Fracking
Infiltration
Self-potential
Localization

SUMMARY

Electrokinetic phenomena are a class of cross-coupling phenomena involving the relative displacement between the pore water (together with the electrical diffuse layer) with respect to the solid phase of a porous material. We demonstrate that electrical fields of electrokinetic nature can be associated with fluid leakages from wells. These leakages can be remotely monitored and the resulting signals used to localize their causative source distribution both in the laboratory and in field conditions. The first laboratory experiment (Experiment #1) shows how these electrical fields can be recorded at the surface of a cement block during the leakage of a brine from a well. The measurements were performed with a research-grade medical electroencephalograph and were inverted using a genetic algorithm to localize the causative source of electrical current and therefore, localize the leak in the block. Two snapshots of electrical signals were used to show how the leak evolved over time. The second experiment (Experiment #2) was performed to see if we could localize a pulse water injection from a shallow well in field conditions in the case of a heterogeneous subsurface. We used the same equipment as in Experiment #1 and processed the data with a trend removal algorithm, picking the amplitude from 24 receiver channels just after the water injection. The amplitude of the electric signals changed from the background level indicating that a volume of water was indeed flowing inside the well into the surrounding soil and then along the well. We used a least-square inversion algorithm to invert a snapshot of the electrical potential data at the injection time to localize the source of the self-potential signals. The inversion results show positive potential anomalies in the vicinity of the well. For both experiments, forward numerical simulations of the problem using a finite element package were performed in order to assess the underlying physics of the causative source of the observed electrical potential anomalies and how they are related to the flow of the water phase.



## 1. Introduction

Various types of fluid leakages that may potentially occur near a wellbore are shown in Fig. 1. This involves flow through the steel casing of a well, through the cement, or along the casing/cement interface, the cement/formation interface, or within a set of microfractures in the cement sheath. Our goal is to develop methods to diagnose such fluid leakage occurrences and to localize them over time. Some of these leakages can be associated with brittle deformation and with the generation of acoustic or seismic emissions, which can be measured remotely and inverted to localize the seismic source (position and moment tensor). While this is said, some leakages may be completely aseismic. Therefore, other methods are required to detect and localize these aseismic events.

The flow of pore water after a hydraulic fracturing operation and associated fluid leakages near the wellbore area results in measurable voltages both during field operations in reservoir environments (Entov et al., 2010; Chen et al., 2011), in shallow aquifers (Wishart et al., 2008), or associated with artificial seismic sources (Kuznetsov et al., 2001). Similar conclusions have been reached in volcanic environments where fluctuations of the electrical field can be observed at the surface of the Earth associated with natural

* Corresponding author at: Colorado School of Mines, Dept. of Geophysics, Green Center, 1500 Illinois Street, 80401 Golden, CO, USA.
*E-mail addresses:* arevil@mines.edu (A. Revil), maodeqiang@gmail.com (D. Mao), mygeophysics@gmail.com (A.K. Haas), marios.karaoulis@gmail.com (M. Karaoulis), lfrash@mymail.mines.edu (L. Frash).

http://dx.doi.org/10.1016/j.jhydrol.2014.12.003
0022-1694/

fracturing processes (e.g., Byrdina et al., 2003). In porous media, the current density generating these self-potential anomalies is associated with the occurrence of the flow of the formation water in saturated or unsaturated conditions. The coupling is electrokinetic in nature, that is associated with the advective transport of the excess (or deficiency) of electrical charges in the pore water. This excess or deficiency of electrical charges is there to compensate for the deficiency or excess of electrical charges on the mineral surface.

There is also a growing literature base related to laboratory observations of electromagnetic fields associated with hydromechanical disturbances (Moore and Glaser, 2007; Wang et al., 2011; Haas et al., 2013; Revil and Jardani, 2013). A complete theory of these electrokinetic effects (that is associated with the relative displacement between the formation water and the rock matrix) has been developed by Mahardika et al. (2012) and Revil and Mahardika (2013). Alternatively, the same types of coupled methodology between hydromechanical and electrical disturbances can be used to identify the presence of microcracks in porous media using a spectral approach (Jougnot et al., 2013), to identify tidal effects in the deformation of glaciers (Kulessa et al., 2003), to perform hydraulic conductivity tomography using a joint inversion of self-potential and head data (Soueid Ahmed et al., 2014), or to infer large scale ground water flow in volcanic edifices (Byrdina et al., 2013).

Beside passive seismic, we are not aware of any other method able to remotely monitor instantaneously fluid leakages in the vicinity of a well. Recently, electrographic methods have been developed as a way to localize hydromechanical events from their electromagnetic signatures (Crespy et al., 2008; Mahardika et al., 2012; Revil and Mahardika, 2013; Haas et al., 2013). This idea is very similar to what is performed in electroencephalography to localize the causative current source of the electrical field fluctuations recorded on the scalp of a human patient or an animal. In biological situations, these currents are associated with the opening of ionic channels at the synapses between the neurons. A variety of deterministic and stochastic techniques have been developed in electroencephalography and in magnetoencephalography to address the inversion or localization problems. The approaches we will follow in this paper are not fundamentally distinct to what has been proposed in medical science (see Grech et al., 2008 for a review of these methods).

In this paper, we present and model two controlled experiments. The first experiment (Experiment #1) is performed in the laboratory and is a follow-up of the experiment described in Haas et al. (2013). Our goal is to analyze the position of two electrical bursts and to show how the localization of the causative source moves over time in the vicinity of the well. The second experiment (Experiment #2) corresponds to a small scale field experiment in which a water pulse was injected at a shallow depth of 65 cm. Electrical potential fluctuations are monitored at surfaces of the cement block in Experiment #1 or at the ground surface in Experiment #2 using a very sensitive voltmeter developed for electroencephalography. Our goal is to show that these electrical (self-) potential signals can be used to localize the pulse injection of water using stochastic or deterministic localization techniques. We call this localization approach "electrography". In addition, we perform numerical modeling using a finite element package in order to explain the laboratory data in terms of a water flow model and to demonstrate the consistency between the streaming potential hypothesis and the observations.

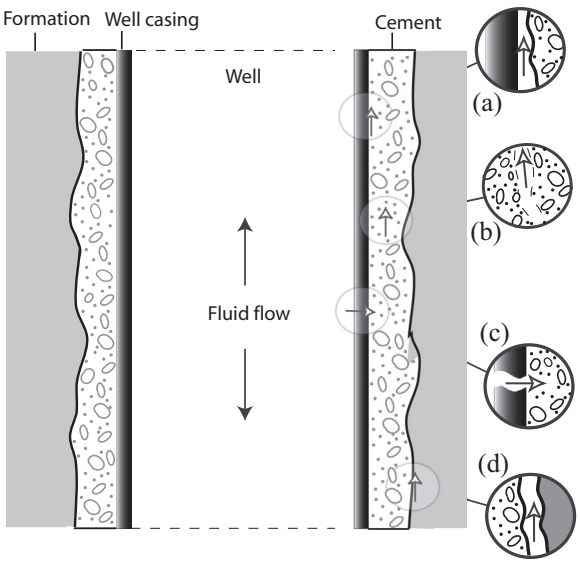


**Fig. 1.** Sketch showing the different possibilities for leakage from a well. Case (a) corresponds to the existence of cracks in between the steel casing and the cement sheath. Case (b) corresponds to the existence of microcracks in the cement. Case (c) corresponds to the existence of pathways directly in the steel casing of the well. Finally case (d) corresponds to the formation of microfractures between the cement and the geological formations. Adapted from Alberta Energies Utility Board, see http://www.psehealthyenergy.org/data/PSE__CementFailureCausesRateAnalaysis_Oct_2012_Ingraffea.pdf.

## 2. Physical concepts

In order to understand the type of electrical field anomalies associated with the leakage from a well (see Fig. 1), we need first to provide a description of the most probable type of mechanisms that can generate such anomalies. We will demonstrate below in Sections 3.5 and 4 that our observations are in agreement with an electrokinetic mechanism, which involves the relative displacement between the charged grains of a poorus material and the pore water. Electrokinetic coupling mechanisms between the hydromechanical equations and the electromagnetic equations are described in Mahardika et al. (2012) and Revil and Mahardika (2013) including dynamic terms related to inertial effects in the continuity and constitutive equations (Newton's and Darcy's laws). The governing equation for the occurrence of self-potential signals is obtained by combining a constitutive equation with a continuity equation. The constitutive equation corresponds to a generalized Ohm's law for the total current density $\mathbf{j}$ (A m$^{-2}$) (e.g., Sill, 1983),

$$\mathbf{j} = \sigma \mathbf{E} + \mathbf{j}_S, \tag{1}$$

where $\sigma$ denotes the low-frequency electrical conductivity of the porous material (in S m$^{-1}$), $\mathbf{E} = -\nabla\varphi$ ($\varphi$ denotes the electrical potential expressed in V) the electrical field in the quasi-static limit of the Maxwell equations for which $\nabla \times \mathbf{E} = 0$ ($\mathbf{E}$ in V m$^{-1}$) and electromagnetic induction is therefore neglected. The first term on the right side of Eq. 1 represents the conduction current density, and the second term represents the kinetically driven source current density (streaming current density). The source current density is given by $\mathbf{j}_S = \hat{Q}_V \mathbf{u}$ where $\mathbf{u}$ denotes the Darcy velocity and $\hat{Q}_V$ the excess of charge (of the diffuse layer) per unit pore volume of the porous or fractured material (in C m$^{-3}$) that can be dragged by the flow of the formation water. More precisely $\mathbf{u}$ (in m s$^{-1}$) denotes the flux of the water phase with respect to a Lagrangian framework associated with the deformation of the skeleton of the porous material. At high flow rates, the flow can be influenced by the value of the Reynolds number for the pervasive flow through the porous material; the case of high Reynolds numbers (>1 but smaller than 200) has been analyzed by Bolève et al. (2007).

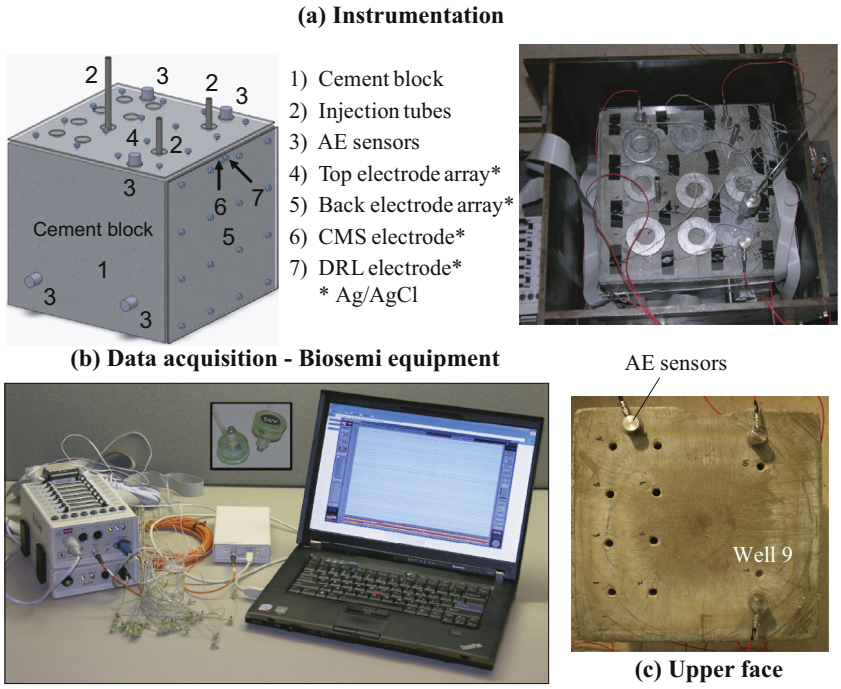


**Fig. 2.** Experimental setup and equipment. a. Instrumentation of the porous block showing the position of the wells, the acoustic emission (AE) sensors, the top and back arrays of non-polarizing elecrodes, and the position of the DRL and CSM electrodes. The cube is ($x$ = 305 mm × $y$ = 305 mm × $z$ = 275 mm). b. Data acquisition system showing the BioSemi electroencephalographic multichannel voltmeter and the laptop computer used for the acquisition as well as the fiber optic cord (in orange) and the small Ag/AgCl sintered electrodes used as probes for the electrical potential measurements. The voltmeter uses 32 of these Ag/AgCl sintered electrodes for the measurement and monitoring of the self-potential anomalies. C. Upper face of the cement block showing well #9 and the three AE sensors. (For interpretation of the references to color in this figure legend, the reader is referred to the web version of this article.)

Eq. 1 can be combined with the following conservation equation for the charge, also given here in the quasi-static limit of the Maxwell equations in which the time derivative of the charge density of free charges is neglected. This conservation of charge is written as,

$$\nabla \cdot \mathbf{j} = 0. \tag{2}$$

Combining Eqs. 1 and 2 yields a Poisson equation for the self-potential $\varphi$ (expressed in V),

$$\nabla \cdot (\sigma \nabla \varphi) = \mathfrak{I}, \tag{3}$$

where $\mathfrak{I}$ denotes the volumetric current density (in A m$^{-3}$). This volumetric current density is given by (e.g., Revil and Jardani, 2013),

$$\mathfrak{I} \equiv \nabla \cdot \mathbf{j}_S = \hat{Q}_V \nabla \cdot \mathbf{u} + \nabla \hat{Q}_V \cdot \mathbf{u}. \tag{4}$$

Eq. 4 together with specific boundary conditions for the electrical potential or the electrical field and Darcy velocity (or fluid pressure) provides the basis to model the occurrence of self-potential signals associated with the flow of water. Therefore, the computation of the "streaming" or "self-" potential, $\varphi$, first requires solving the water flow problem, a task that will be undertaken below in this paper.

## 3. Experiment #1: Monitoring leakage in a cement block

Our first controlled experiment is a laboratory experiment. The goal is to localize two data snapshots in the electrical potential distribution associated with the rupture of the seal of a well in a failed attempt to hydraulically fracture a cement block using water injected into the well. Localizing several events, we can follow the evolution of the leak between the well and the cement that corresponds to leakage mechanisms a, b, and d in Fig. 1 over time. The forward modeling for this experiment is discussed in Section 4 in which we show that the main direction of flow is parallel to the casing.

### 3.1. Materials and methods

The porous material used for Experiment #1 is a cement mixture (FastSet Grout Mix) with a porosity of 0.31, a dry density of 1950 kg m$^{-3}$, and a Young modulus of 10 GPa (Hampton et al., 2013). This cement was cured for about 10 months before the experiment. The porous sample has a cubical shape ($x$ = 30.5 cm × $y$ = 30.5 cm × $z$ = 27.5 cm, see Fig. 2a and c). After curing, several 10 mm diameter holes (well #1 through #10) were drilled into the block to varying depths such that various sealing methods could be tested (Fig. 2c). Stainless steel tubing with 9.5 mm outside diameter was placed into a few holes using Loctite Instant Mix 5-Minute epoxy as the casing sealing agent. The electrodes were attached to the top and one side of the block (16 electrodes on each face, 32 electrodes in total). The electrodes (1 mm in diameter, see Fig. 2a) were solid sintered silver with a solid AgCl coating. Each electrode has a voltage amplifier built into the electrode casing. The electrodes were electrically connected to the block surface through a drop of conductive gel usually used for electroencephalography. Six acoustic emission sensors were also mounted to three faces of the block (Fig. 2c) and additional information regarding the acoustic emission sensors and the localization of the acoustic emissions is discussed in detail in Frash (2012), Hampton (2012), Frash et al. (2012), and Hampton et al. (2013).

The electrical response during the experiment was measured using a very sensitive multichannel voltmeter manufactured by BioSemi, Inc., that was originally designed for electroencephalography (http://www.biosemi.com/, see Fig. 2b). The electrode potentials were measured using the BioSemi ActiveTwo data acquisition system that is self-contained, battery powered, galvanically isolated, and digitally multiplexed with a single high sensitivity analog to

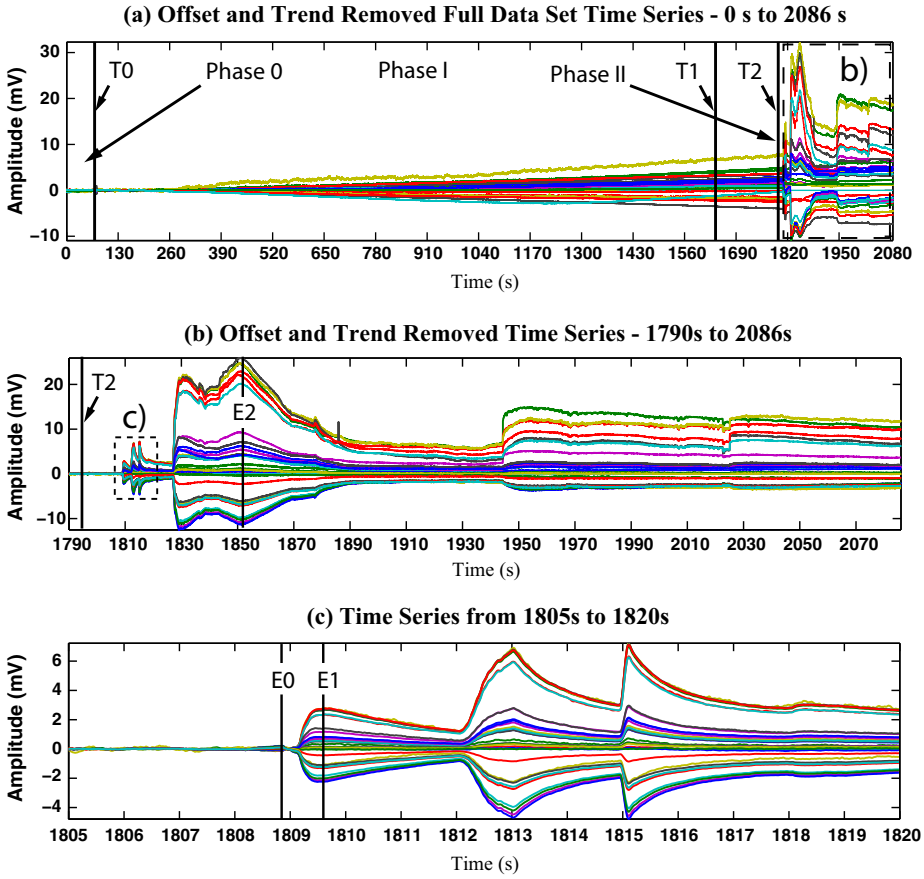


**Fig. 3.** Self-potential time series associated with the injection of saline water in Hole #9. a. Full time series data set showing the different fluid injection time periods during data acquisition (T0, T1, and T2). Phase 0 corresponds to the preinjection data. Phase I corresponds to the fluid pressure buildup in the well. Phase II corresponds to a set of breakage and pulse flow events between the well and the cement. Event E0 denotes the first event (see Fig. 6a) associated with a seismic event that may correspond to a progressive seal failure. Note the significant change in electrical response after T2 that is bounded by region after 1820 s. b. Zoom highlighting the background normalized electrical response (detrended time series) showing distinct electrical impulses related to the start of constant flow injection at T2 with selected peak event E2. c. Zoom highlighting the first series of impulsive signals including the selected peak events E0 and E1.

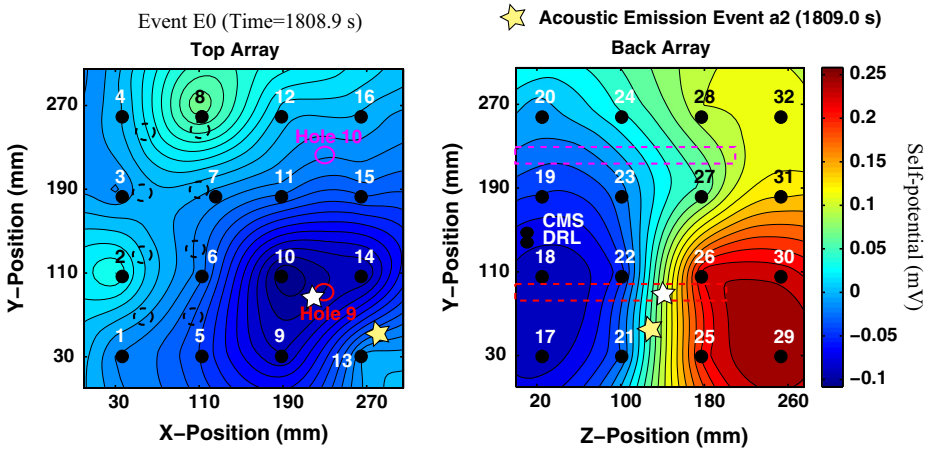


**Fig. 4.** Self-potential spatial voltage distributions of Event E0 (see Fig. 3) corresponding to the first seismic event corresponding to the initiation of the seal failure. This event, however, does not happen at the outlet of Well #9 but at a depth of roughly 14 cm (see the white star symbol in the figure). The yellow star denotes a seismic event occurring at the same time (see Table 1). Note that the self-potential anomaly is relatively small in magnitude (compare with Fig. 5) and is negative on the top of the cube and positive in its lower part (below $z = 150$ mm) displaying a dipolar anomaly with an electrical field that is stronger at a depth of about 140 mm. (For interpretation of the references to color in this figure legend, the reader is referred to the web version of this article.)

digital converter per measurement channel. Additional information regarding the BioSemi system can be found in Crespy et al. (2008), Haas and Revil (2009), Ikard et al. (2012), and Haas et al. (2013). The apparatus we used has 32 channels, a sensitivity of 1 nV, and an input impedance of 100 MΩ. This apparatus can support up to 256 channels and the time delay between channels is 1 picosecond.

All of the digitized data is referenced to the Common Mode Sense (CMS) electrode (which is not recorded), in a dynamic feedback loop with the actively driven Driven Right Leg (DRL)

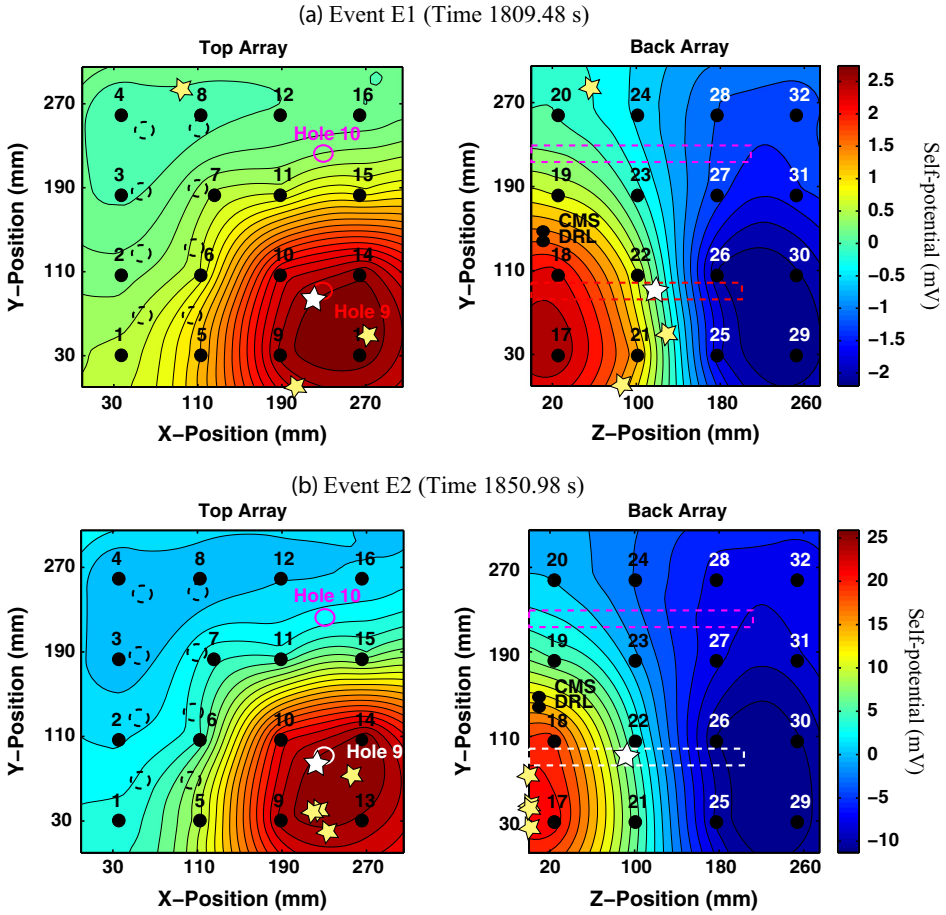


**Fig. 5.** Self-potential spatial voltage distributions of Events E1 and E2. a. Event E1: voltage distribution showing the peak voltage associated with the second hydraulic pulse during constant flow injection. Note the voltage polarities in the spatial distributions and the color bar voltage scale (+2.5 mV to −2.0 mV). Event E1 represents the second of a series of electrical field bursts. b. Spatial voltage distribution for Event E2 showing the peak voltage associated with the highest magnitude pulse during constant flow injection. The white star corresponds to the inverted position of the dipole responsible for the observed self-potential anomaly while the yellow stars indicate the acoustic emission localizations. These self-potential events E1 and E2 are stronger in magnitude than event E0 (see Fig. 4) and are reversed in magnitude). (For interpretation of the references to color in this figure legend, the reader is referred to the web version of this article.)

electrode. The BioSemi voltmeter replaces the "ground" (reference) electrodes which are used in conventional self-potential acquisition systems with these DRL and CMS electrodes. These electrodes form a feedback loop, which drives the average potential on the surface of the porous cube (the Common Mode voltage) as close as possible to the ADC reference voltage in the AD-box of the voltmeter. This CMS/DRL loop has two additional functions: First, the effective impedance of the DRL electrode is decreased with a factor of 100 at 50 Hz because of the feedback loop. This results in a 40 dB extra CMRR at 50 Hz when compared with using normal ground electrodes with the same impedance. Second, the DRL electrode is the only current return path between the subject and the AD-box. The return current is limited electronically at 50 μA. With the BioSemi voltmeter, each electrode or a combination of electrodes can be used as the "reference" for the self-potential map (this choice is made in the acquisition software). The raw digitized data represents a fully differential data set, and is saved directly on a laptop computer during the acquisition (Fig. 2b). Because this data set is differential with respect to the CMS electrode, none of the recorded channels represent a reference potential in the system. To establish a properly referenced data set, one channel must be subtracted from all of the others (http://www.biosemi.com/). In our measurements we selected the least active signal in the data set (Channel #4) as the reference for the display of the electrical potential maps. In other words, this channel will correspond to the zero potential to which the self-potential maps will be referenced. The entire system, including the computer, is operated on batteries to minimize electromagnetic couplings with the electrical power system.

### 3.2. Results

During the experiment, the cement block was in equilibrium with the atmospheric conditions in the laboratory (~30% relative humidity and 83 kPa absolute pressure). Saline water containing 10 g of NaCl dissolved into 1000 ml of deionized water (conductivity of 1.76 S $m^{-1}$ at 25 °C) was used as the fracturing fluid injected. The fluid control system injected fluid through stainless steel tubes (Fig. 2) using a computer controlled Teledyne Isco 100DX syringe pump with precise flow rate or pressure control. The injection tube was cased along the upper interval to a depth of 16.4 cm and an open hole interval was drilled after the epoxy seal cured to a total depth of 19.4 cm, giving a 3.0 cm open hole interval. The system had a total fluid capacity of 103 ml, and was capable of achieving pressures up to 68.9 MPa while maintaining constant flow rates of 0.001–60 mL $min^{-1}$. A constant fluid flow rate of 1.0 mL $min^{-1}$ was then imposed on the system with the intent of inducing hydraulic fracturing. Under constant flow, either the cement block or the tubing seal would eventually fail if the injection rate is sufficiently higher than flow in the cement matrix.

For the experiment associated with Hole #9 (see Fig. 2c), a 60 s pre-injection (termed Phase 0) electrical potential measurement

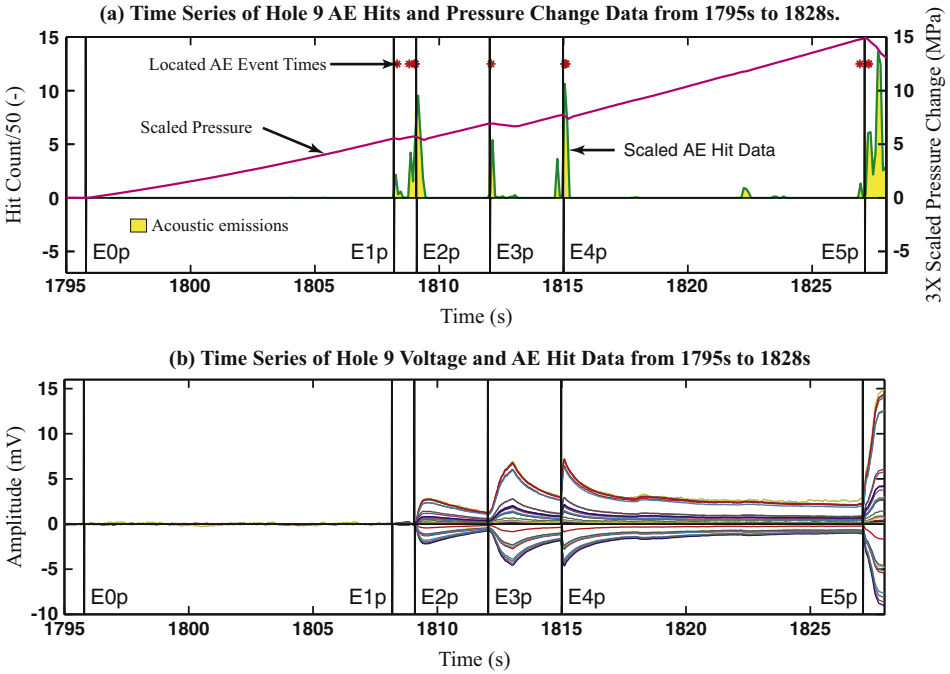


**Fig. 6.** Fluid pressure, acoustic emissions, and electrical potential changes during a given time window. a. The Acoustic Emission (AE) data and fluid pressure change correlation. The red asterisks denote the located acoustic emission events. b. The voltage responses at all 32 self-potential stations. The events labeled E0p–E5p represent the same events in each panel of the figure. The acoustic emission hits, the pressure changes, and the initiation of changes in the voltage data all align, indicating that there is some causal relationship between these phenomena.

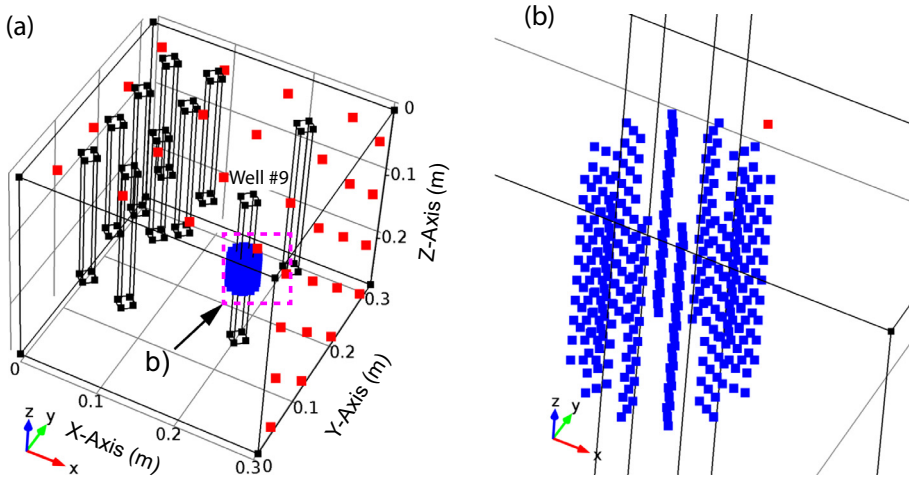


**Fig. 7.** Comsol geometry used for the fine geometry kernel matrix computations (360 positions) in the localization problem. a. Finer resolution cylindrical kernel matrix point distribution (blue squares) along with the measurement points used with the genetic algorithm (red squares) around Hole #9. We also show the different wells existing in the cement block (see Fig. 1d). b. Close up of the kernel matrix point distribution around Hole #9. (For interpretation of the references to color in this figure legend, the reader is referred to the web version of this article.)

period was acquired (Fig. 3a). The goal of this phase was to establish individual channel offsets and drift trends for use during post acquisition signal processing. Constant pressure fluid injection at 1.17 kPa (termed Phase I) was initiated at T0 = 60 s and terminated at T1 = 1632 s. This phase was followed by Phase II, a 1.0 ml/min constant flow rate initiated at T2 = 1795 s (note that fluid pressure was maintained, but not actively controlled between T1 and T2). Fluid injection was terminated well after the end of the electrical data acquisition, when seal failure was confirmed through the appearance of water on the surface of the block near the injection hole.

Fig. 3 shows the temporal evolution of the electrical potential for all of the electrodes. There are seven major events of which three are highlighted (see Figs. 3–5). Events E1 and E2 are used below to test our localization procedure. These events are shown in the time series of Fig. 3. All major electrical potential events occurred during Phase II constant flow injection. During Phase I, the measured electrical potential gradually increased as fluid was injected into the cement block. No bursts in the electrical field were observed during the constant pressure phase (Phase I, see Fig. 5).

Each major event was characterized by a rapid change in the electrical potential time series followed by a slower exponential-type relaxation of the potential with a characteristic time comprised between several seconds to several tens of seconds (Fig. 3). This relaxation was believed to be associated with the

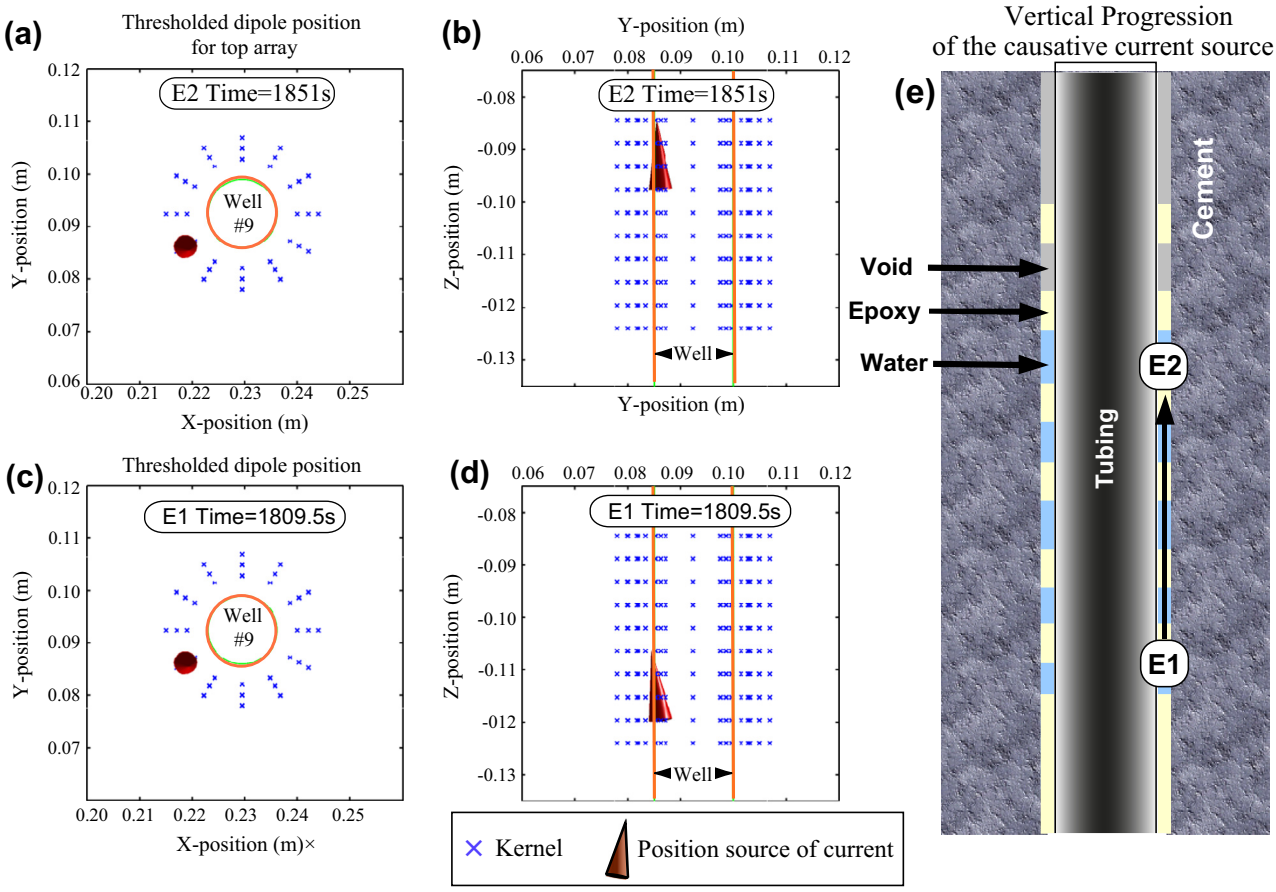


**Fig. 8.** Proposed explanation of the electrical disturbances observed in the experiment. Events E1 and E2 are localized near Hole #9 in panels a. to d. The blue ×'s in panels denote the dipole point positions used to compute the kernel. The circle in panels (a) and (c) represents the position of Hole #9 as viewed from the top, and the vertical red lines in panels (b) and (d) represent the position of Hole #9 as seen from the side. e. Conceptualization of the movement of the fluid through multiple epoxy barriers, filling voids in between each barrier with water. The voids represent points of open contact with the cement that allow the fracturing fluid to make direct contact, generating the observed pressure fluctuations, electrical impulses, and possibly the acoustic emissions. It can be clearly seen in this figure that the first event, E1, occurs lower in the model representation (and by correlation, in the test specimen) than the later event, E2. For Event E1, the main dipole is located at ($x$ = 21.8 cm, $y$ = 9.2 cm, $z$ = −11.9 cm) with a magnitude $M_1$ = 0.2 mA m while for Event E2, the location is at ($x$ = 21.8 cm, $y$ = 9.2 cm, $z$ = −9.7 cm) with a magnitude $M_2$ = 1.6 mA m. (For interpretation of the references to color in this figure legend, the reader is referred to the web version of this article.)

relaxation of the fluid pressure as discussed further below. Because the relaxation of the potential distribution was relatively slow after each event, a sequence of overlapping events causes a superposition of the potentials from each event in the sequence to varying degrees (see Fig. 3b and c). We will discuss in Section 3.5 these overlappings when we will assess the value of the streaming potential coupling coefficient.

Fig. 4 shows the self-potential distribution associated with the Event E0, which was the first seismic event recorded on the acoustic emission sensor array due to constant flow injection. Ordinary spatial kriging was performed on each face separately. We show later how we can determine the depth of this event, yet it is clear from simply looking at the distribution of the equipotentials that the centroid of the event is at a depth of about 14 cm (in the center of the dipole). We will show that the potential distribution is also consistent with a downward flow of the fluid.

The snapshots corresponding to Events E1 and E2 are shown in Fig. 5. Note that the distribution of the electrical potentials is reversed with respect to Event E0. The evolution of the fluid pressure at the inlet of Hole #9 and acoustic emissions is shown in Fig. 6. The acoustic emission hit counts peaked very close to and during the pressure changes. This is an indication that a breakage occurred resulting in a momentary pressure drop during these times. The sequence is highly temporally correlated, and indicates breakage associated with electrical bursts, followed by periods of

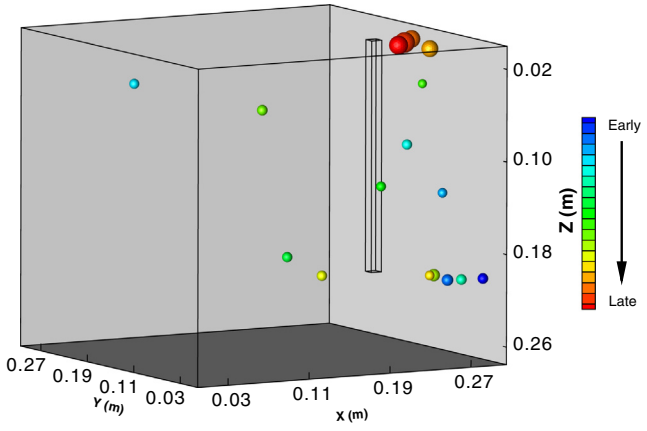


**Fig. 9.** Localization of the acoustic emission data in the porous cube for different time windows (data from Table 1). For the events localized close to Well 9, we can see that the acoustic emission sources are moving up from the bottom to the top of the cube.

low acoustic emission activity and relaxation of the electrical potential anomalies. The electrical data provides information related to the flow process during the series of events in progress. Each of the pressure drops shown in Fig. 6a indicates that the seal

**Table 1**
Acoustic emission events. ($x$, $y$, $z$) denotes the position of the source, $q$ is a data quality indicator comprised between 0 (poor quality) to 1 (well localized), $A$ denotes the amplitude of the event, and t is the time of the event.

| Event | $x$ (mm) | $y$ (mm) | $z$ (mm) | $q$ (–) | $A$ (dB) | $t$ (s) |
|---|---|---|---|---|---|---|
| a0 | 280 | 6 | 200 | 0.14 | 32 | 1808.32 |
| a1 | 245 | 6 | 199 | 0.00 | 35 | 1808.81 |
| a2 | 268 | 55 | 132 | 1.00 | 29 | 1809.01 |
| a3 | 93 | 281 | 52 | 0.87 | 30 | 1809.03 |
| a4 | 207 | 10 | 80 | 1.00 | 31 | 1809.06 |
| a5 | 257 | 3 | 199 | 0.00 | 32 | 1812.10 |
| a6 | 222 | 52 | 0 | 0.59 | 25 | 1814.73 |
| a7 | 198 | 200 | 199 | 1.00 | 31 | 1815.06 |
| a8 | 209 | 58 | 122 | 1.00 | 30 | 1815.07 |
| a9 | 291 | 130 | 47 | 0.35 | 27 | 1815.12 |
| a10 | 223 | 287 | 84 | 0.26 | 32 | 1826.93 |
| a11 | 228 | 0 | 193 | 0.67 | 37 | 1827.28 |
| a12 | 257 | 243 | 224 | 1.00 | 31 | 1827.29 |
| a13 | 224 | 0 | 193 | 0.94 | 29 | 1827.49 |
| a14 | 238 | 25 | 1 | 0.76 | 51 | 1865.45 |
| a15 | 252 | 81 | 0 | 0.99 | 53 | 1866.21 |
| a16 | 228 | 51 | –2 | 0.91 | 62 | 1868.73 |
| a17 | 222 | 51 | 0 | 0.13 | 57 | 1868.80 |

is progressively failing (not full failure with a single critical event), resulting in the burst-like behavior observed in Fig. 3.

### 3.3. Source localization of the electric disturbances

For a conductive half space, the electrical potential distribution at an observation point $P$ is given by (e.g., Revil and Jardani, 2013):

$$\varphi(P) = \frac{1}{2\pi}\int_{\Omega}\rho(M)\frac{\nabla\cdot\mathbf{j}_S(M)}{x(P,M)}dV + \frac{1}{2\pi}\int_{\Omega}\nabla\ln\rho(M)\cdot\frac{\mathbf{E}(M)}{x(P,M)}dV, \quad (5)$$

where $x$ denotes the distance from the source at position $M$ to the electrode located at position $P$ (observation point) where the electrical potential signal $\varphi(P)$ is recorded, and $\rho(M)$ denotes the electrical resistivity around point $M$. In Eq. 5, the two contributions associated with the primary field (first term of the right-hand side of Eq. 5) and the secondary potential (the second term of the right-hand side of Eq. 5) are separated. The primary source term is due to the hydromechanical disturbances while the second term is due to the heterogeneities in the resistivity distribution of the resistive block.

Another way to write the solution in a more compact form is given in Eq. 6,

$$[\varphi_i] = K_{ij}[\mathbf{j}_j], \quad (6)$$

where $[\varphi_i]$ $(1 \leqslant i \leqslant N)$ denotes the vector of self-potential observations ($N$ denotes the number of stations used for the monitoring), $\mathbf{K}$ (with components $K_{ij}$) is called the kernel or the leading field matrix ($N \times 3M$) ($M$ is the number of cells used to discretize the conductive medium in which the source of current are localized), and $[\mathbf{j}_j]$ corresponds to the $3 \times M$ vector of the source current density at each cell $j$ $(1 \leqslant j \leqslant 3M)$. The elements of the kernel are the Green's functions that connect the self-potential data at a set of $P$ measurement stations located at the measurement surface, and the $M$ sources of current density at a defined set of source points located within the conducting volume. The kernel computation accounts for the electrical resistivity distribution within the volume of interest and the boundary conditions applied to the system. In the following computations, we will use a uniform resistivity distribution within the domain volume except at the position of the holes drilled into the block. These holes are considered as very high impedance zones within the volumetric resistivity distribution, and are explicitly accounted for in the computation of the kernel. We do not account for the resistivity change associated with the formation of the cracks. Indeed, this change in resistivity is difficult to estimate and it is spatially localized and therefore it is not expected to play a big role on the fluctuations of the self-potential field distribution at the surface of the block.

The philosophy we are following for the inversion and localization of the causative source current density is based on the following steps: We first use a deterministic method on a coarse grid covering the entire cube. Since the self-potential inversion problem is linear, it converges quickly to a distributed source current solution (few iterations are however required using a minimum support regularizer to compact the source current density). Once

**Table 2**
Maximum variations in the recorded self-potential signals and fluid pressure in Well #9 during the rupture events E2p to E5p.

| Seismic event | $\Delta p$ (MPa) | $\Delta\varphi$ (mV) |
|---|---|---|
| E2p | 0.33 | 3.5 |
| E3p | 0.67 | 5.0 |
| E4p | 0.27 | 4.0 |
| E5p | 1.00 | 12.0 |

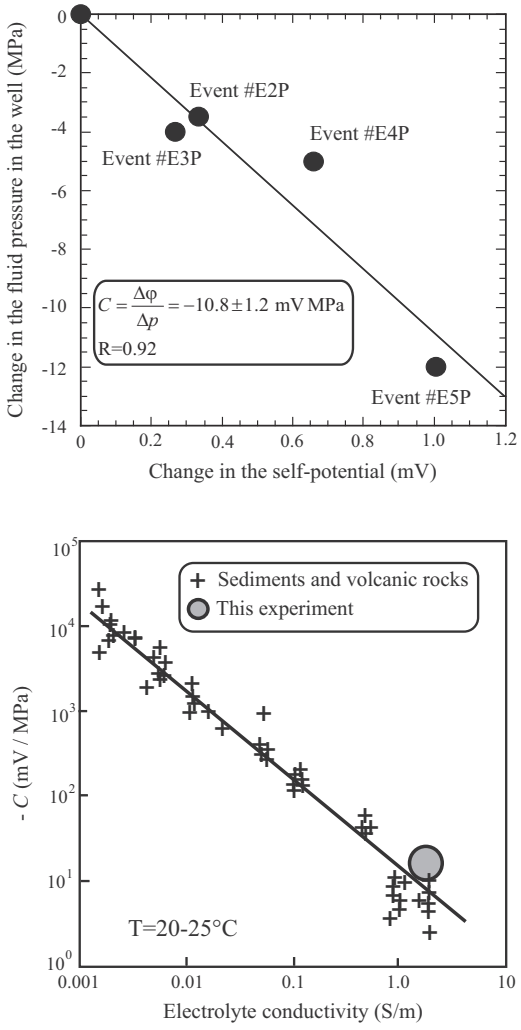


**Fig. 10.** Determination of the streaming potential coupling coefficient. For a set of four events (see Fig. 6a, the maximum change in the electrical potential is linearly correlated to the change in the fluid pressure in Hole #9. The lower figure shows that the recovered value of the streaming potential coupling coefficient is consistent with a broad variety of measurements at different salinities. This indicates that the nature of the coupling is electrokinetic, and therefore related to the flow of formation water within the porous block.

**Table 3**
Parameters used in the numerical model.

| Seismic event | $K$ (m/s) | $S_S$ (1/m) | $\sigma$ (S/m) |
|---|---|---|---|
| Cement/epoxy | $1.16 \times 10^{-10}$ | $8.0 \times 10^{-1}$ | $1.0 \times 10^{-3}$ |
| Crack | $1.16 \times 10^{-4}$ | $8.0 \times 10^{-4}$ | $1.0 \times 10^{-2}$ |

the localization of the causative source of current has been roughly localized, we switch to the much more numerically costly genetic algorithm using a fine grid only in the region found at step 1. The direct use of a genetic algorithm on a fine grid covering the complete cube would be very computationally expensive to do. This procedure is elegant and efficient and can be considered as a way to combine the advantages of deterministic and stochastic algorithms (e.g., Mester et al., 2011).

The gradient-based approach indicates that the causative source of the observed signals is located in the vicinity of Well #9. To refine the localization, we used a single dipole genetic algorithm-based search through a fine kernel matrix with 360 positions (Fig. 7). Electrography, though the use of the genetic algorithm, is conducted as follows. A population of candidate dipole solutions is used to find the solution of the inverse problem. This population has to evolve toward solutions that minimize the data misfit function,

$$P_d(\mathbf{m}) = \|\mathbf{d} - \mathbf{Km}\|_2^2, \tag{7}$$

where $\|cdot\|_2$ refers to the L2 norm and **K** denotes the kernel. The model vector **m** used in the inverse model contains $360 \times 3 = 1080$ elements (the number 360 represents the number of position in the kernel while the number 3 represents the three components of each current dipole moment vector). For each generation, the goodness of fit is evaluated through the data misfit objective function described by Eq. 7. Multiple individuals are stochastically selected from the current population and modified to form a new population. This new population is then used at the next iteration. The process is continued until a predetermined number of generations is reached or a satisfactory data misfit has been reached. We used the genetic algorithm in Matlab (Global optimization toolbox,

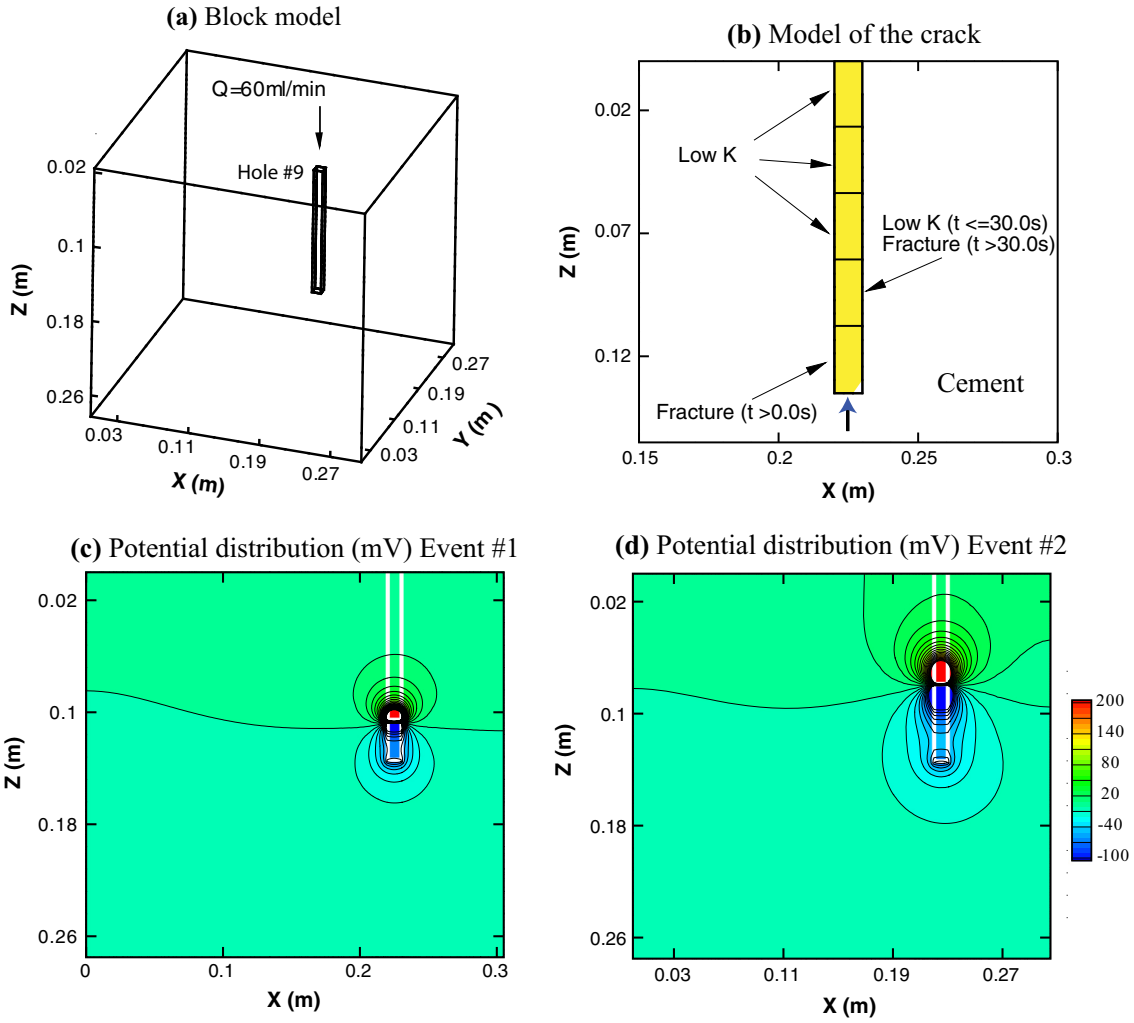


**Fig. 11.** Numerical modeling of the laboratory experiment. a. Sketch of the simulation domain. The whole block represents the cement and is used for the simulation of self-potential response. The strip inside the cement block denotes the flow simulation domain. It corresponds to the potential location of a propagating crack. Injection Well#9 is not included in the simulation and is only simulated by a hydraulic flux boundary at the bottom of the simulation domain (the flow of water is therefore going upward). b. Cross-section view of the flow domain (in yellow), which is discretized into five zones. At $t = 0.0$ s, a high conductivity zone with $K = 1.16 \times 10^{-4}$ m s$^{-1}$ to represents the existing crack and at $t = 30$ s, the $K$ of the zone above the crack is changed from $1.16 \times 10^{-10}$ m s$^{-1}$ to $1.16 \times 10^{-4}$ m s$^{-1}$ to mimic the extension of the crack under the build-up of the fluid pressure. c. and d. Simulated self-potential anomaly inside the block indicating that a dipole is formed at the boundary between low and high hydraulic conductivity zones in the flow domain. The snapshots correspond to before and after the formation of a new fracture. (For interpretation of the references to color in this figure legend, the reader is referred to the web version of this article.)

Mathworks (2012a), http://www.mathworks.com/products/global-optimization/functionga.m).

The results of the localization are shown in Fig. 8 for Events E1 and E2. We clearly identified the events as localized in the vicinity of the well. Also, the vertical progression of the leak along the well between these two temporally sequential snapshots can clearly be seen in Fig. 8. The two localizations are separated by a distance of roughly 2.2 mm. To analyze whether this distance is meaningful, we went back to the whole set of permissible solutions provided by the genetic algorithm and we found that each localization has an uncertainty of 1 mm in the three directions. Therefore our results are encouraging because they clearly show that we can monitor these events over time with a good precision.

### 3.4. Source localization of the acoustic emissions

We used AEwin software, developed by Physical Acoustics Corporation (PAC), to perform the source location analysis of the acoustic emissions. This software uses regression analysis to calculate event locations based on triggering (i.e., pre-defined amplitude threshold crossing) time. Samples are recorded at 1 MHz and band-pass filtered to 1–400 kHz. This software reports error with a correlation coefficient ($q$ is comprised between 0 for a poor localization to 1 for a precise localization) rather than a distance estimate (AE sources were typically located within 0–10 mm if the respective $q$ was greater than 0.9).

The localization of the acoustic emissions is shown in Fig. 9 and the events are described in Table 1. The localizable events are mostly clustered around Well #9, but not close to the well. This may indicate that these correspond to the reactivation or failure of cracks located further away in the concrete specimen. That said, we see a clear evolution of the position of the events with time from the lower part of the specimen up to the surface close to the inlet of Well #9. This agrees with visual observation of brine leakage through the well annulus to the inlet at the top surface of the specimen. Visual confirmation of leakage was observed 3–8 min after well pressures indicated initial breakdown (Event E0 and a0).

### 3.5. Nature of the coupling mechanism

In order to proceed to the numerical modeling of the observed phenomenon (discussed in Section 4 below), we need to be sure that the coupling mechanism responsible for the observed self-potential anomalies is electrokinetic in nature. This can be accomplished by first checking the maximum change in the electrical potential (before and after) each of the seismic events shown in Fig. 6b. Using this figure, we can also estimate the drop in the fluid pressure recorded in Well #9. For the four events shown in Fig. 6a, these values are reported in Table 2 and Fig. 10. The ratio of the change in the electrical potential to the change in the formation fluid pressure denotes the streaming potential coupling coefficient $C$

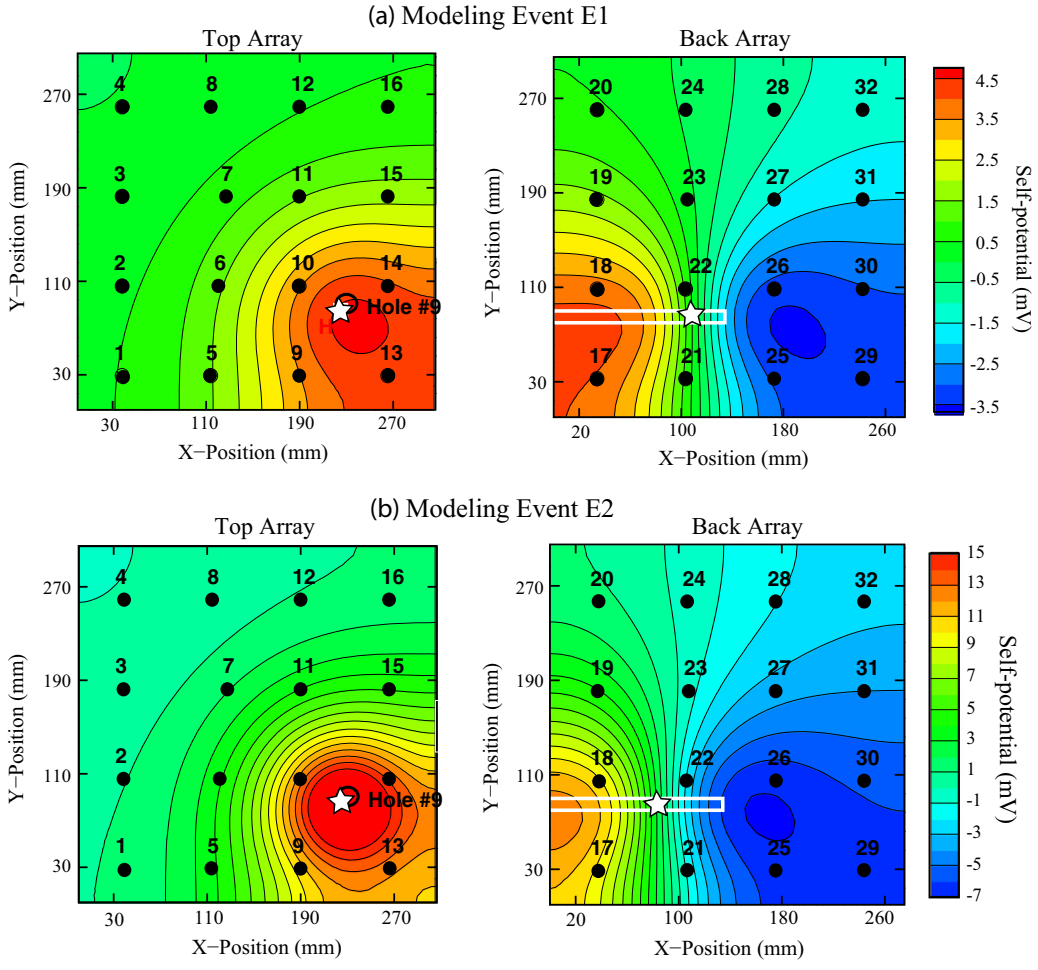


**Fig. 12.** Self-potential spatial voltage distributions resulting from the simulated flow in a fracture. a. Event E1. b. Event E2. The white star shows the position of the tip of the crack. This figure can be compared to Fig. 5 corresponding to the real data. In these figures, we can see the effect of the source getting closer to the top electrode array. The white rectangle corresponds to the projection of the flow domain (see Fig. 11b) while the white star corresponds to the exact position of the tip of the crack.

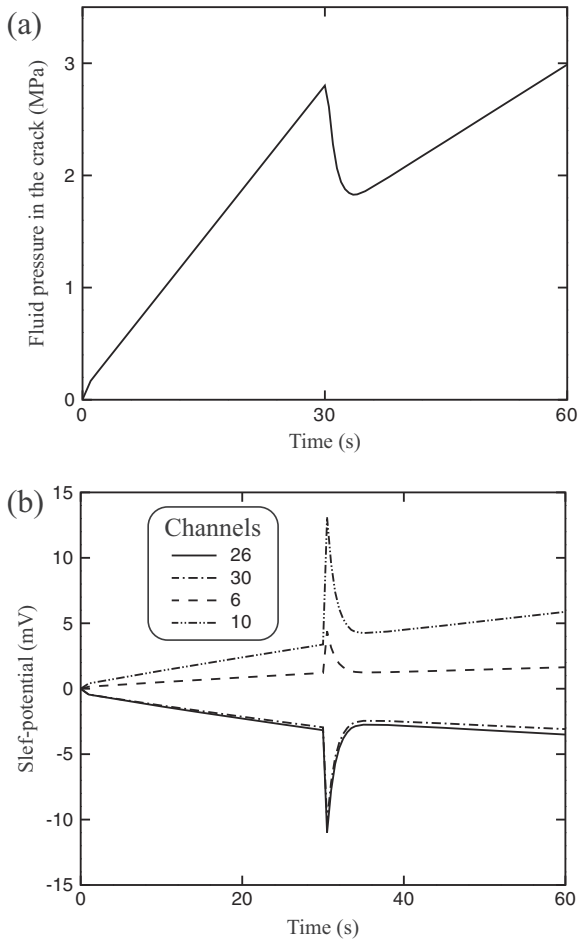


**Fig. 13.** Fluid pressure change and associated self-potential response during the creation of a crack and the associated disturbance in the formation water flow. a. The formation of a crack generates a fluid pressure release at the injection well very similar to the experimental data recorded in the laboratory experiment. b. With the drop of pressure, there is also a corresponding burst in the electrical fields, which can be numerically observed at different locations on the surface of the block (here at stations 6, 10, 26, and 30, see position Fig. 12). Note that the self-potential time series have not been detrended and therefore cannot be directly compared to the times series shown in Fig. 3.

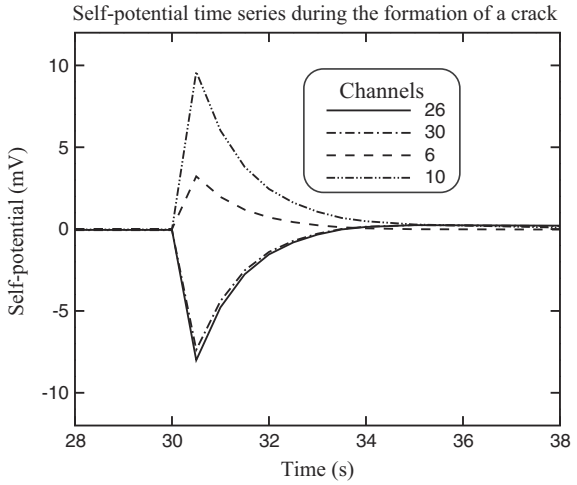


**Fig. 14.** De-trended self-potential time series highlighting the influence of the formation of the crack. The formation of a fracture is accompanied by a burst in the electrical field and an exponentially decaying tail associated with the relaxation of the fluid pressure produced with the flow of the formation water.

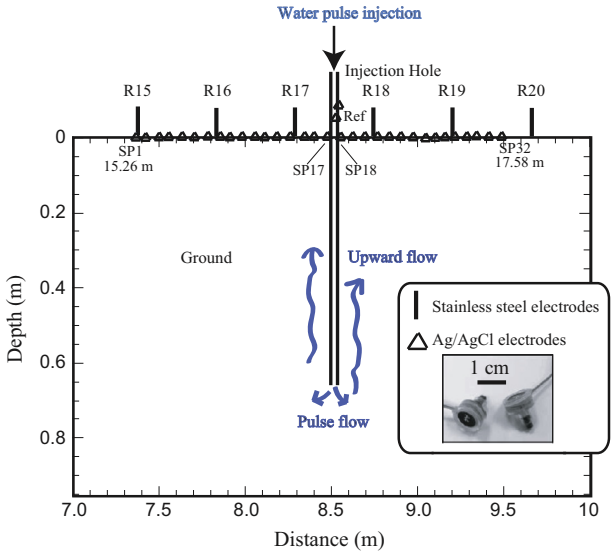


**Fig. 15.** Experimental setup for Experiment #2. The non-polarizing electrodes were emplaced around the injection well. The well consists of a plastic tube with an open end localized at a depth of 65 cm from the ground surface. The self-potential data were collected with a 32-channel ultrasensitive voltmeter (BioSemi). The distance between the Ag–AgCl electrodes is 7.5 cm and the well is localized between electrode SP17 and SP18. The two reference electrodes are located roughly 10 cm from to the well on one side with respect to the profile shown in this figure. R15 to R20 denote the position of some of the electrodes used for resistivity tomography. The water flow comes from the outlet of the well but then flows in the vicinity of the well until it is observed to reach the ground surface.

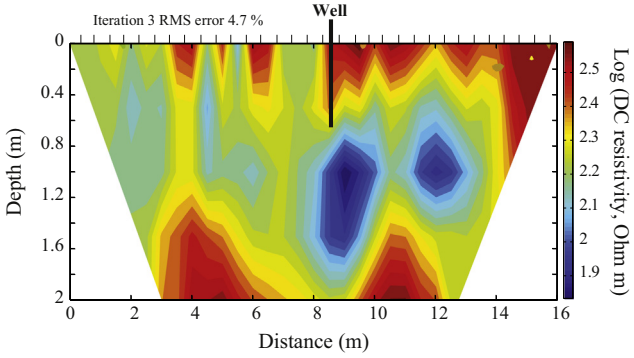


**Fig. 16.** Electrical resistivity tomogram prior the pulse injection. Inverted DC-resistivity section using the Gauss–Newton method. The data are collected using 32 electrodes with 50 cm spacing.

$$C = \left(\frac{\partial \varphi}{\partial p}\right)_{\mathbf{j}_S=0}. \tag{8}$$

We obtain a value of $C$ equal to $-10.8 \pm 1.2$ mV MPa$^{-1}$, which is consistent with data in the literature (e.g., Revil et al., 2003, their Fig. 3) showing the effect of the salinity upon the coupling coefficient (Fig. 10). In the present case, the conductivity of the brine is 1.76 S m$^{-1}$ at 25 °C.

## 4. Numerical modeling of the laboratory experiment

The goal of this section is to = model part of the underlying physics of the self-potential anomalies associated with ten formation of new cracks and therefore to strengthen the interpretation of the observations reported in Section 3. As discussed above in Section 3.3, the electrical source responsible for the observed

self-potential anomaly is localized in one side of the injection well and the source current density for each new event moved upward with increasing applied pressure over time. For the following numerical simulation, we attempted to simulate the dipolar self-potential response recorded in the experiment as well as the burst in the electrical field associated with the opening of a crack from a hydrogeological perspective.

### 4.1. Numerical model configuration

The numerical simulations are based on the theory discussed in Section 2 above. The simulation domain for the self-potential response represents the whole cement block, 30.5 cm × 30.5 cm × 27.5 cm. For the water flow domain, however, we only have chosen a narrow 1.0 cm × 1.0 cm × 13.5 cm strip near the injection well. There are two reasons for this choice. First, we only observed water coming out of the location near the injection well, not from other areas within the cement block. Secondly, compared to fracturing the cement, it is easier to fracture the epoxy located between the well and the cement. This has been shown through the inversion of the self-potential data (see previous section). Because we are dealing with flow in microcracks, we perform the flow simulation in 2D away from the well, solving the flow equations in transient conditions. The flow problem is characterized by the diffusion equation,

$$\frac{\partial p}{\partial t} - \frac{S_S}{K}\nabla^2 p = F \tag{9}$$

where $p$ is the fluid pressure (in Pa), $S_S$ the specific storage ($m^{-1}$), $K$ the hydraulic conductivity ($m\ s^{-1}$), and $F$ is the source term (if positive, in $s^{-1}$) or sink term (if negative). Inside the flow domain, we consider two different regions, the crack itself and epoxy/cement undamaged zones. We assign a larger hydraulic conductivity, specific storage, and electrical conductivity (injected water with high salinity) to the crack itself by comparison with the undamaged zone. We will see later in this section that these changes of properties are responsible for some asymmetry in the resulting potential distribution for the dipole. The parameters used in the simulation can be found in Table 3. The modeling is done in two steps: 1 We assume the region at the bottom is the initial crack, and has a pressure profile that increases with time. We simulate the electrical potential associated with this pressurization profile. 2 Finally, we simulate the creation of a new crack at $t = 30$ s (see Fig. 11a and b). This simulation is not fully coupled to the mechanical problem. In other words, we decide arbitrarily when the crack is formed and then we compute the effect on the flow of the water and finally the electrical potential response.

In the numerical simulation, we assume an initial hydrostatic flow condition with a pressure head equal to zero at the top of domain (Fig. 11b), and it is also assumed that the flow domain is fully water-saturated (we consider the resistivity of the cement to be 1000 Ω m). The disturbance from the initial pressure distribution can be ignored compared with the high injection pressure. The bottom of the flow domain is assigned a flux boundary with a total flow rate of 60 mL $min^{-1}$. All the other boundaries are assumed to have no flow boundaries. The flow is therefore one dimensional in essence and the only outlet corresponds to the constant pressure boundary condition imposed at the top of the flow domain (Fig. 11b).

For the self-potential simulation, we assume ground at electrode 4, the same one used as the reference electrode in the laboratory experiment. All of the external boundaries of the model are in contact with an insulating material and therefore the normal component of the electrical field vanishes at these boundaries. For the self-potential simulation, the holes drilled in the cement and the influence of steel well casings were not considered. Indeed, the steal casing is entirely wrapped using resistive epoxy and its influence is anticipated to be small. In our model, the electrical conductivity of the epoxy is assumed to be the same as the cement (1000 Ω m). The simulation only involves the constant rate injection part of the experiment; we did not attempt to include the constant pressure part (Phase 0) at the beginning of experiment.

### 4.2. Simulation of the dipolar anomaly

With the injection of water at the bottom of the flow domain, there is a hydraulic gradient at the interface between the microcrack and undamaged zone of the flow domain. In other regions, the hydraulic head drop is smaller. Therefore, the water is forced to flow at the tip of the fracture and because of the drop in the electrical and hydraulic properties at the tip of the microcrack, we expect the generation of a strong self-potential anomaly (see Eq. 4).

What we obtained with the model is very similar to the dipole response from the laboratory experiment, shown in Fig. 5. The location of the dipole in the model is right at the interface between the crack and the undamaged zone (Fig. 11b), in other words at the tip of the crack. The pattern of the self-potential anomaly can be observed on the top and back sides of the block in Fig. 12. Note the similarities between Figs. 5 and 12. On the top surface, we note a positive anomaly more or less centered close to the injection well

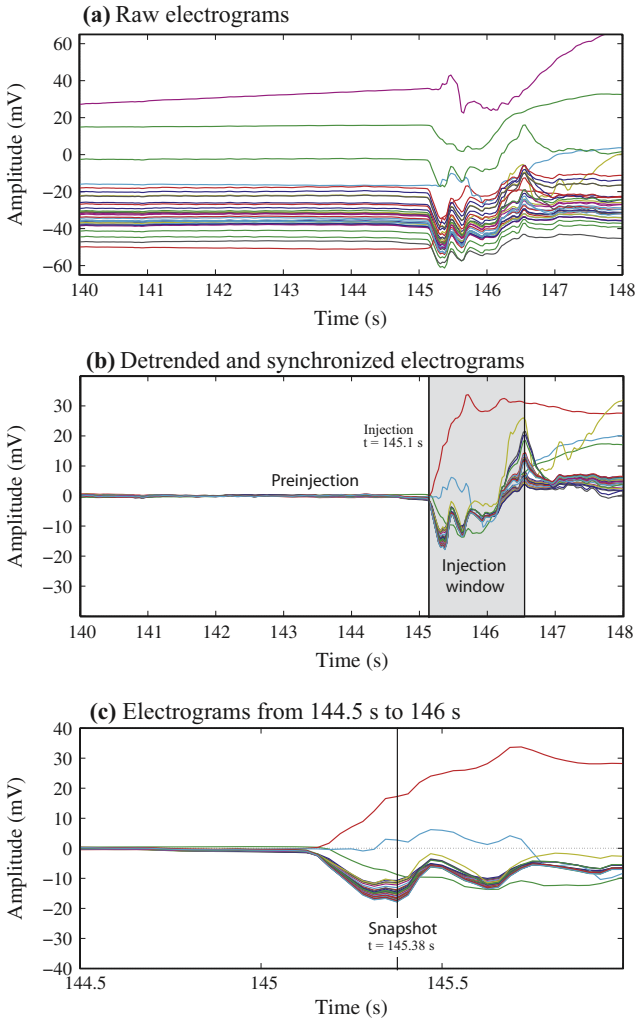


**Fig. 17.** Self-potential time series from the water injection experiment. a. Raw electrograms. b. Detrended and background corrected electrograms. c. Magnification of the electrograms showing the preinjection and injection time windows.

and a negative self-potential anomaly on the bottom part the cement block. Because of the involvement of high salinity water from the injection (10 times greater than the cement and epoxy), the negative lobe of the dipole has a smaller amplitude than the positive side, which is consistent with the laboratory observations (see Fig. 5).

### 4.3. Creation of a new crack

Figs. 11b–d and 12–14 show the self-potential signals associated with the development of a new crack in the numerical model. At the start of the simulation, we only have one crack at the bottom of the flow domain. At time $t = 30.0$ s, we suddenly change the hydraulic conductivity, specific storage, and electrical conductivity of the zone just above the interval to simulate the creation of a new crack in the flow domain. Fig. 11c and d show the distribution of the self-potential signals along a slice crossing the cube and Hole #9. We clearly see the dipolar nature of the self-potential distribution due to the water flowing through the tip of the crack. Fig. 12 shows the distribution of the self-potential signals corresponding roughly to Event E1 and E2. These potential distributions are qualitatively in good agreement with the self-potential distributions observed in Fig. 5.

The variation of the fluid pressure at the injection point is illustrated in Fig. 13a while Fig. 13b exhibits the self-potential signals at 4 electrodes on the surface of the cube (2 from the top surface and 2 from the side). These 4 locations are used to mimic the electrode response shown in Fig. 3. It is evident that there is a significant pressure drop in the well (see Fig. 6 for the laboratory experiment) and a concomitant burst in the self-potential response associated with the opening of the tip of the crack and the generation of a new crack. For the data displayed in Fig. 13b, each curve has two components: one is related to the continuous injection of water and second related to the generation of a new crack. A constant and continuous injection rate will create a quasi-linear variation in self-potential signals. We simply remove this trend from the curves as was done for the real dataset using fourth-order polynomial (Fig. 13b). The detrended curves are shown in Fig. 14, which displays characteristics that are very similar to the real data shown in Fig. 3. From the detrended curves, we clearly see the burst recorded at the different locations on the external surface of the cube with a large response for the electrodes near the event and a smaller response for the electrodes located further away. However, compared to the laboratory data, the relaxation time following the burst is shorter. This can be attributed to the process for creating a new crack that extends from the old crack. We instantaneously introduce a high hydraulic conductivity zone to simulate the new crack in the numerical simulation. In reality, it may take a few seconds to create a new fracture and the relaxation would depend on how the fluid pressure gets dissipated by the water flow. This localized pressure dissipation is a function of the opening size between the old and new fracture. A small opening (relative to the crack interface area) would slow down the fluid transfer to the new crack, which increases the relaxation time.

## 5. Experiment #2: Pulse injection in the field

The goal of the second experiment is to describe a small field case study in which a water pulse is injected into a very shallow well, and the electrical potential fluctuations are recorded at the ground surface and inverted to localize where the pulse of water occurred.

### 5.1. Materials and methods

The experimental setup is shown in Fig. 15, and consists of a plastic tube in which water was injected for 1.4 s with a flow rate of 0.6 L $s^{-1}$. The self-potential response during the experiment was

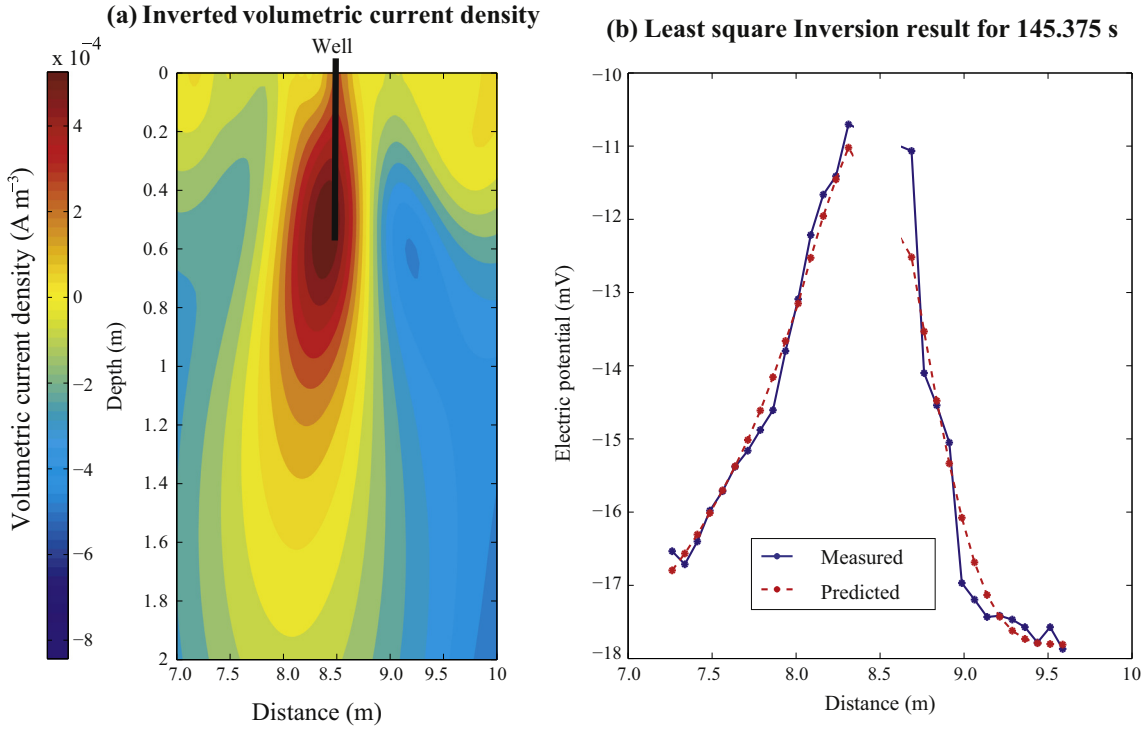


**Fig. 18.** Source localization of a single snapshot at time 145.375 s the localization of the self-potential anomaly (positive pole associated with the pulse injection). a. Source current density distribution shown at the third iteration of the inversion process. The maximum of the source current density is located very closely to the end of the open well. The electrical resistivity has been accounted for this inversion. b. Comparison between the measured self-potential signals at the ground surface and those reconstructed using the current density shown in Panel a. Note that the three channels showing spurious signals in Fig. 17 have been ignored.

recorded with the same equipment described above. In the experiments, the electric potential measurements were acquired with 32 amplified non-polarizing silver-silver chloride (Ag AgCl) electrodes with a spacing of 7.5 cm along a rectilinear profile. The sampling rate was 300 Hz. The water pulse injection occurred during the time window 145.15–146.55 s. By putting the well in the ground with a hammer, we probably created vertical flow paths between the well and the soil as sketched in Fig. 15 that will likely lead to vertical flowpaths associated with leaking.

Two DC resistivity profiles were also evaluated before prior and after the water injection test with the ABEM SAS-4000 Terrameter impedance meter. The DC resistivity profile comprised a total of 32 stainless steel electrodes (50 cm spacing) and 118 measurements with the Wenner array electrode configuration. The apparent resistivity data were inverted with RES2DINV 3.4 (Loke and Barker, 1996). The electrical resistivity tomogram is shown in Fig. 16. This resistivity tomogram is used below to invert the self-potential data to localize the causative source in the subsurface.

### 5.2. Results

The full time series of the self-potential measurements (called electrograms, see Crespy et al., 2008) are shown in Fig. 17. They are taken for a time window between 140 and 148 s in the entire data set. We used a linear trend removal process on all of the time series data for all the 32 channels to establish the same base line during the pre-injection time window shown in Fig. 17. The results are shown in Fig. 17b and c. A snapshot of the self-potential distribution is shown in Fig. 18b. It shows a negative baseline and a positive anomaly on the top of this baseline. The negative baseline corresponds to the fact that the CMS and DRL electrodes are located close to the injection well. What is really important is the positive anomaly, which amounts to between 6 and 8 mV and is centered on the injection well. This anomaly is inverted in the next section to localize the source current density responsible for this anomaly.

### 5.3. Localization

We describe now the algorithm used to localize the causative current density distribution associated with the self-potential anomaly observed in this second experiment. We will show in Section 5.4 that a deterministic approach is good enough to point out the position of the outflow associated with the water injection. Eq. 6 can be written in a matrix form as $\mathbf{d} = \mathbf{K}\mathbf{m}$ where $\mathbf{m}$ is a vector containing the $M$ source of the volumetric current density terms $\Im$, $\boldsymbol{d}$ denote the vector of electric potentials $\varphi$ observed at $N$ electrodes, and $\mathbf{K}$ is the kernel matrix corresponding to $\Im = \nabla \cdot \mathbf{j}_S$ rather than $\mathbf{j}_S$ (see Section 5.3). Therefore the dimension of $\mathbf{K}$ is $N \times M$. The data misfit vector is defined by

$$\mathbf{e} = \mathbf{K}\mathbf{m} - \mathbf{d}, \tag{10}$$

The objective function to minimize is expressed as (Jardani et al., 2008)

$$\mathrm{P}^{\alpha} = \|\mathbf{W}_d\mathbf{e}\|_2^2 + \alpha\|\mathbf{W}_m\mathbf{m}\|_2^2, \tag{11}$$

where $\mathbf{W}_\mathrm{d}$ correspond to the data ($N \times N$) weighting matrix, $\mathbf{W}_m$ to the ($M \times M$) model covariance matrix (we use the Laplacian operator to ensure smoothness), $\|\|_2^2$ denotes square of the L2 norm, $\alpha$ is the regularization parameter. The least square solution corresponding to $\partial \mathrm{P}^{\alpha}/\partial \mathbf{m} = 0$ is given by

$$\mathbf{m} = \left[\mathbf{K}^T(\mathbf{W}_d^T\mathbf{W}_d)\mathbf{K} + \alpha(\mathbf{W}_m^T\mathbf{W}_m)\right]^{-1}\left(\mathbf{K}^T(\mathbf{W}_d^T\mathbf{W}_d)\mathbf{d}\right). \tag{12}$$

The value of the regularization parameter, $\alpha$, is determined using the L-curve approach with the regularization parameter in the range of $[10^{-3}, 10^{3}]$ (see Jardani et al., 2008). We obtain $\alpha = 0.121$ as the optimized parameter for this case. In our model, we have $M = 8241$ and $N = 28$ (4 noisy channels were removed from the dataset). The kernel is computed in 3D by extending the 2D resistivity distribution in the strike direction.

### 5.4. Application

We applied the algorithm discussed in Section 5.3 to a snapshot of the self-potential data. The result of the inversion is shown in Fig. 18 after three iterations. The tomogram shows a positive distribution of the volumetric current density $\Im$ located close to the end of the open well where the pulse water injection takes place (Fig. 18a). This source current density reproduces the data with a RMS error of 0.12 mV (Fig. 18b) and the causative source is centered on the outlet of the well. Therefore we have successfully determined the location of the pulse injection in the ground.

## 6. Numerical modeling of the field experiment

The purpose of this numerical model is to try to replicate the self-potential signals observed in the field experiment. Since most of water did not flow into the ground and was observed to be forced to flow along the space between the tubing of the well and the soil. We simulate water in a narrow strip along the injection well by assigning a higher hydraulic conductivity to that area. Like in the simulation of the laboratory experiment, the domain configuration for the simulation of the self-potential signals is also

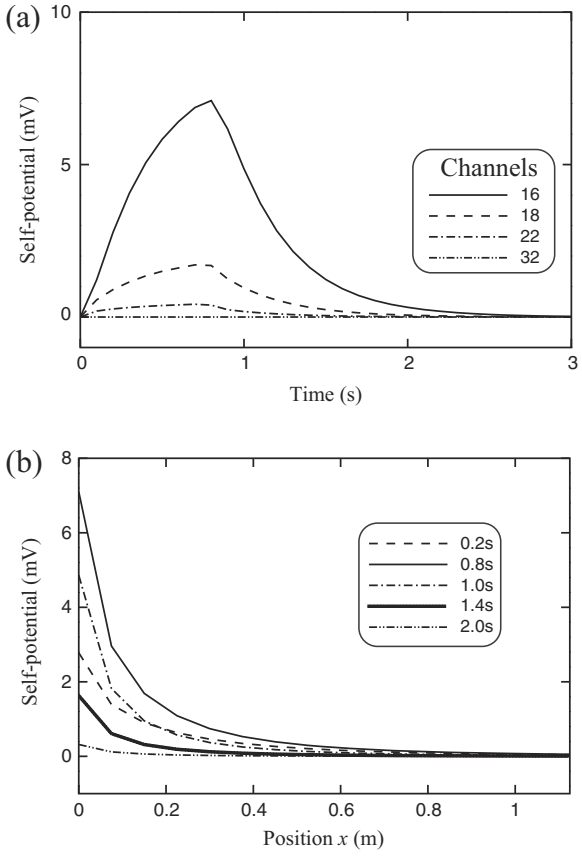


**Fig. 19.** The upper figure shows the changes in self-potential as a function of time for four different electrodes. The bottom figure corresponds to surface self-potential profiles at different times following the end of the injection. The maximum potential difference along each side of the current source is roughly 7 mV from the injection point out to a point that is one meter or more away from the well. In the lower figure, the $x$-axis position origin is at the center of the point of injection.

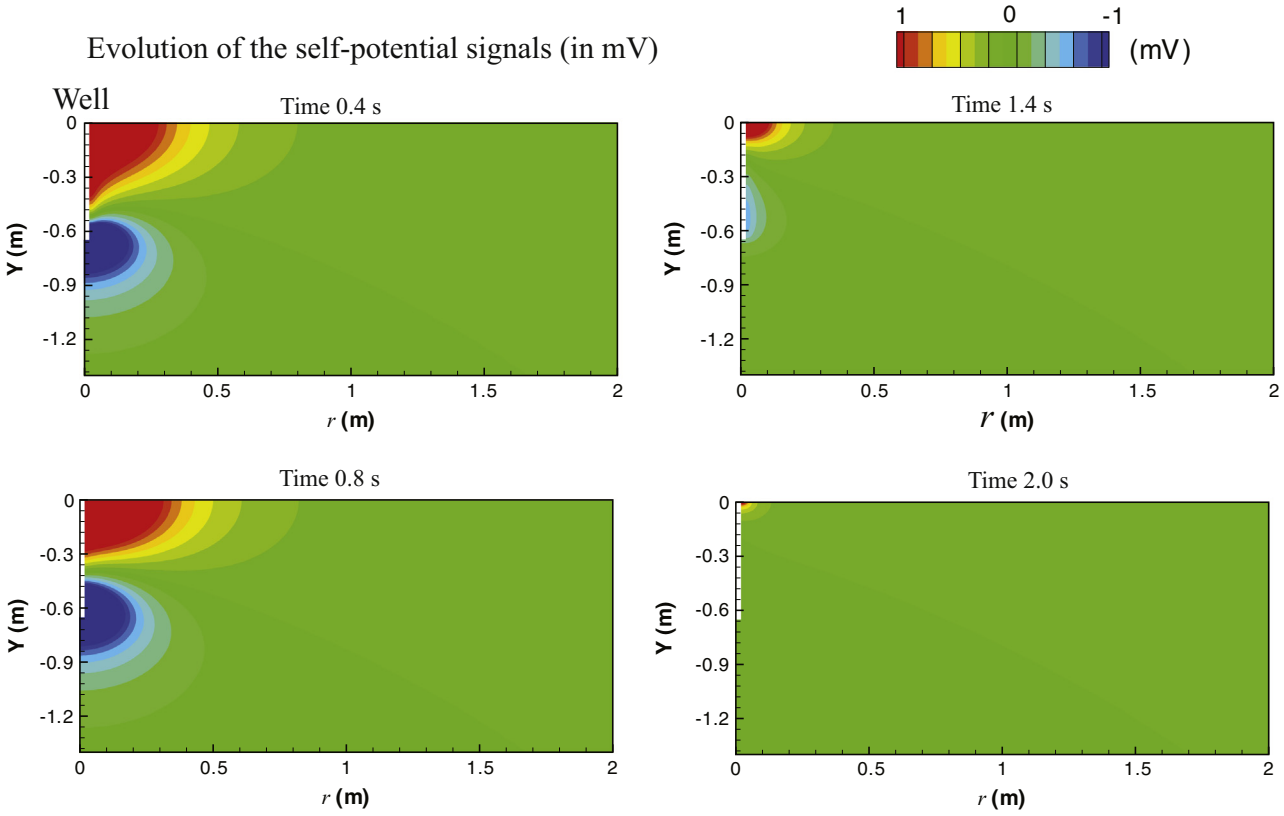


**Fig. 20.** Numerical simulation of the vertical self-potential contour maps at time 0.4 s, 0.8 s, 1.4 s and 2.0 s with respect to the radial direction $r$ from the injection well (located at $r = 0$ m). Since the array is located at the ground surface, it can observe only the positive anomaly associated with the upward of the formation water along the well.

important. The simulation domain of the 2D axisymmetric model for the self-potential simulations is 6 m by 3 m. We assigned a flux boundary with the magnitude of 1 L s$^{-1}$ at the bottom of the flow domain and zero pressure at the top of the flow domain (2 cm wide along the well). The simulated velocity field is coupled with the self-potential model for the calculation of the external current density. Since the flow in the strip is like a fracture flow, a very high hydraulic conductivity ($K = 0.046$ m s$^{-1}$) is assigned to the flow domain with a high specific storage ($S_S = 0.1$ m$^{-1}$). For the self-potential model, a constant electrical conductivity ($\sigma = 0.003$ S m$^{-1}$) has been assigned throughout the domain.

The self-potential response at various times for four different electrodes is shown in Fig. 19a. The signals increase to a peak at 0.8 s corresponding to the end of the water injection in the well. The self-potential signals then relax back to zero over time. In Fig. 19b, we show a radial self-potential profile at several time periods. The difference along each profile could be used for inverse modeling.

Fig. 20 shows the self-potential contour map in the model domain at different times. Clearly, the self-potential has a dipole pattern, and what is observed in Fig. 19 is the positive anomaly close to the well. The negative anomaly in the model exists below the injection point, and is not observable from the surface. Note that in Fig. 17, the self-potential data at different electrodes are displayed with respect to the CMS electrode (of the BioSemi system) used as the data acquisition reference. The positive part of the field data anomaly (146–147 s) represents the portion of the experiment where the water was most likely moving upward, eventually gushing out onto the surface. These numerical model results compare qualitatively well with the positive anomaly portion of the field data.

## 7. Conclusions

Our goal in this paper was to develop a new approach to localize leakages in wells using an electrographic method similar to what has been developed in medical imaging to study brain activity or to identify the source of epilepsy. The first experiment was developed to show that a sequence of electrical bursts associated with the rupture of the seal around a well in cement block can be inverted to localize the causative source. This approach, called electrography, can be used to localize fluid leakages from a well as a function of time. It was applied for the first time to a sequence of events showing the evolution of the leakage with time. Two of these events were numerically simulated and it was found that water flow through the tip of the crack generated a dipolar anomaly that can be remotely measured with a network of electrodes. If we have several events occurring more or less at the same time and therefore a superposition of the self-potential distributions associated with these events, we could, here again, borrow some approaches from electroencephalography to separate the effects associated with the different events (such a principal component analysis in space and time).

The second experiment was designed to show that a pulse water injection in a heterogeneous natural soil can be detected with a multichannel voltmeter connected to a network of electrodes located at the ground surface. In both cases, the resulting electrical potential distribution can be inverted to localize the causative current source while taking into account the resistivity distribution of the material. In the first experiment, electrography was performed with a stochastic method (the genetic algorithm) while in the second experiment, it was conducted using a deterministic method. Electrography opens the door to the detection

and monitoring of fluid leakages in the shallow subsurface in real time. The advantage of the method is that the equipment is relatively cheap in comparison with seismic equipment and that the method can be extended to allow real-time monitoring and analysis. A potential disadvantage of the presented approach is that the self-potential signals can be small, which makes it challenging to detect them from the ground surface, especially in presence of significant amount of electromagnetic noise.

## Acknowledgements

We thank the Colorado School of Mines Unconventional Natural Gas and Oil Institute (UNGI) CIMMM Consortium sponsors for the support of this research. The opinions expressed in this paper are those of the authors. We thanks J.A. (Sander) Huisman and two referees for their very constructive reviews.

## References

Bolève, A., Crespy, A., Revil, A., Janod, F., Mattiuzzo, J.L., 2007. Streaming potentials of granular media: Influence of the Dukhin and Reynolds numbers. J. Geophys. Res. 112, B08204. http://dx.doi.org/10.1029/2006JB004673.

Byrdina, S., Friedel, S., Wassermann, J., Zlotnicki, J., 2003. Self-potential variations associated with ultra-long period seismic signals at Merapi Volcano. Geophys. Res. Lett. 30 (22), 2156. http://dx.doi.org/10.1029/2003GL018272.

Byrdina, S., Ramos, D., Vandemeulebrouck, J., Masias, P., Revil, A., Finizola, A., Gonzales Zuniga, K., Cruz, V., Antayhua, Y., Macedo, O., 2013. Influence of the regional topography on the remote emplacement of hydrothermal systems with examples of Tiscani and Ubinas volcanoes, Southern Peru. Earth Planet. Res. Lett. 365, 152–164.

Chen, M.Y., Raghuraman B., Bryant I., Supp, M.G., Navarro J., 2011. Completion Apparatus for Measuring Streaming Potentials and Determining Earth Formation Characteristics. February. U.S. Patent 7,891,417 B2.

Crespy, A., Revil, A., Linde, N., Byrdina, S., Jardani, A., Bolève, A., Henry, P., 2008. Detection and localization of hydromechanical disturbances in a sandbox using the self-potential method. J. Geophys. Res. 113, B01205. http://dx.doi.org/10.1029/2007JB005042.

Entov, V.M., Gordeev, Y.N., Chekhonin, E.M., Thiercelin, M.J., 2010. Method and an Apparatus for Evaluating a Geometry of a Hydraulic Fracture in a Rock Formation: October. U.S. Patent 7,819,181 B2.

Frash, L., 2012. Laboratory Simulation of an Enhanced Geothermal Reservoir. M.S. Thesis. Colorado School of Mines. Golden, Colorado.

Frash, L., Hampton, J., Gutierrez, M., 2012. On the experimental simulation of EGS reservoirs using a heated true-triaxial apparatus. In: Proceedings of New Zealand Geothermal Workshop 2012. 19–21 November 2012. Auckland, New Zealand.

Grech, R., Cassar, T., Muscat, J., Camilleri, K.P., Fabri, S.G., Zervakis, M., Xanthopoulos, P., Sakkalis, V., Vanrumste, B., 2008. Review on solving the inverse problem in EEG source analysis. J. NeuroEng. Rehab. 5 (25), 1–33. http://dx.doi.org/10.1186/1743-0003-5-25.

Haas, A., Revil, A., 2009. Electrical signature of pore scale displacements. Water Resour. Res. 45, W10202. http://dx.doi.org/10.1029/2009WR008160.

Haas, A.K., Revil, A., Karaoulis, M., Frash, L., Hampton, J., Gutierrez, M., Mooney, M., 2013. Electrical potential source localization reveals a borehole leak during hydraulic fracturing. Geophysics 78 (2), D93–D113. http://dx.doi.org/10.1190/GEO2012-0388.1.

Hampton, J., 2012. Laboratory Hydraulic Fracture Characterization using Acoustic Emission. M.S. Thesis. Colorado School of Mines. Golden, Colorado.

Hampton, J., Frash, L., Gutierrez, M., 2013. Investigation of Laboratory Hydraulic Fracture Source Mechanisms Using Acoustic Emission. In: ARMA 13–315, 47th US Rock Mechanics/Geomechanics Symposium Proceedings, San Francisco, CA, USA, 23–26 June 2013, 9 pp.

Ikard, S.J., Revil, A., Jardani, A., Woodruff, W.F., Parekh, M., Mooney, M., 2012. Saline pulse test monitoring with the self-potential method to non-intrusively determine the velocity of the pore water in leaking areas of earth dams and embankments. Water Resour. Res. 48, W04201. http://dx.doi.org/10.1029/2010WR010247.

Jardani, A., Revil, A., Bolève, A., Dupont, J.P., 2008. 3D inversion of self-potential data used to constrain the pattern of ground water flow in geothermal fields. J. Geophys. Res. 113 (B09204), 2008. http://dx.doi.org/10.1029/2007JB005302.

Jougnot, D., Rubino, J.D., Rosas Carbajal, M.R., Linde, N., Holliger, K., 2013. Seismoelectric effects due to mesoscopic heterogeneities. Geophys. Res. Lett. 40. http://dx.doi.org/10.1002/grl.50472.

Kulessa, B., Hubbard, B., Brown, G.H., Becker, J., 2003. Earth tide forcing of glacier drainage. Geophys. Res. Lett. 30 (1), 1011. http://dx.doi.org/10.1029/2002GL015303.

Kuznetsov, V.V., Plotkin, V.V., Khomutov, S.Y., Grekhov, O.M., Pavlov, A.F., Fedorov, A.N., 2001. Powerful seismovibrators as a possible source of acoustic and electromagnetic disturbances. Phys. Chem. Earth Part A. 25 (3), 325–328.

Loke, M.H., Barker, R.D., 1996. Practical techniques for 3D resistivity surveys and data inversion. Geophys. Prospect. 44, 499–523.

Mahardika, H., Revil, A., Jardani, A., 2012. Waveform joint inversion of seismograms and electrograms for moment tensor characterization of fracking events. Geophysics 77 (5). http://dx.doi.org/10.1190/GEO2012-0019.1.

Mester, A., van der Kruk, J., Zimmermann, E., Vereecken, H., 2011. Quantitative two-layer conductivity inversion of multi-configuration electromagnetic induction measurements. Vadose Zone J. 10, 1319–1330.

Moore, J.R., Glaser, S.D., 2007. Self-potential observations during hydraulic fracturing. J. Geophys. Res. 112, B02204. http://dx.doi.org/10.1029/2006JB004373.23.

Revil, A., Naudet, V., Nouzaret, J., Pessel, M., 2003. Principles of electrography applied to self-potential electrokinetic sources and hydrogeological applications. Water Resour. Res. 39 (5), 1114. http://dx.doi.org/10.1029/2001WR000916.

Revil, A., Mahardika, H., 2013. Coupled hydromechanical and electromagnetic disturbances in unsaturated clayey materials. Water Resour. Res. 49 (2), 744–766. http://dx.doi.org/10.1002/wrcr.20092.

Revil, A., Jardani, A., 2013. The Self-Potential Method, Theory and Applications in Environmental Geosciences. Cambridge University Press, 366 pp.

Sill, W.R., 1983. Self-potential modeling from primary flows. Geophysics 48, 76–86.

Soueid Ahmed, A., Jardani, A., Revil, A., Dupont, J.P., 2014. Hydraulic conductivity field characterization from the joint inversion of hydraulic heads and self-potential data. Water Resour. Res. 50. http://dx.doi.org/10.1002/2013WR014645.

Wang, E., He, X., Wei, J., Nie, B., Song, D., 2011. Electromagnetic emission graded warning model and its applications against coal rock dynamic collapses. Int. J. Rock Mech. Min. Sci. 48 (4), 556–564.

Wishart, D.N., Slater, L., Schnell, D.L., Herman, G.C., 2008. Hydraulic anisotropy characterization of pneumatic-fractured sediments using self-potential gradient. J. Contam. Hydrol. 103, 133–144.